JOURNAL OF MATERIALS SCIENCE **37** (2002) 117–126

Densification and strength evolution in solid-state sintering

Part II *Strength model*

XIAOPING XU, PEIZEN LU, RANDALL M. GERMAN
Center for Innovative Sintered Products, P/M Lab, 147 Research West, Pennsylvania State University, University Park, PA 16802-6809, USA
E-mail: rmg4@psu.edu

A compact gains strength in sintering through low-temperature interparticle bonding, followed by further strength contributions from high-temperature densification. On the other hand, thermal softening substantially reduces a compact's strength at high temperatures. Therefore, the *in situ* strength during sintering is determined by the competition among interparticle neck growth, densification, and thermal softening. Distortion in sintering occurs when the compact is weak. Most strength models for sintered materials are semi-empirical relations based on the sintered fractional density. These models do not include microstructure or sintering cycle parameters; thus, they do not provide guidelines for thermal cycle design to improve compact dimensional control. A strength evolution model is derived which combines sintering theories and microstructure parameters, including interparticle neck size, solid volume fraction, and particle coordination number. The model predicts sintered strength and when combined with thermal softening gives a good prediction of *in situ* strength. The validity of the model is verified by comparison to experimental data for sintered and *in situ* strength of bronze and steel powders.

1. Introduction

Sintering starts with shaped powders and produces engineered components via a high temperature thermal process that substantially strengthens the compact. A component can routinely increase strength by a factor of 200 to 500 from the green condition to the sintered state. To transform the loosely bonded particles into a high-performance structure involves many changes that include interparticle bonding, densification, microstructure coarsening, and concomitant strengthening. The evolution of mechanical properties is important to many sintered materials and often provides a basis for evaluation of a sintering process [1]. On the other hand, the *in situ* strength as evolving during sintering has significant impact on both densification and dimensional precision. For example, a low *in situ* strength allows densification, but is associated with distortion. Hence, an improved understanding of strength evolution would assist in optimizing sintering cycles, achieving a good combination of densification and shape retention. Unfortunately, fundamental understanding of sinter strengthening is limited.

Most strength models are semi-empirical and simply express strength in terms of fractional density with little regard to the underlying microstructure [2]. Consequently, these models cannot assist in thermal cycle design for improved dimensional precision in sintered materials. The importance of interparticle neck growth to strength was addressed in prior studies [3–7], but only a few [4, 6] include interparticle neck size.

A new model is presented for strength evolution during sintering. It relies on basic sintering neck growth calculations to predict the sintered and *in situ* strength based on interparticle neck size, solid volume fraction, particle coordination number, stress concentration, and thermal softening. The model is tested using experimental results of strength for both prealloyed Cu-10Sn bronze and mixed elemental Fe-2Ni-0.9C steel powders. The *in situ* strength during sintering depends on the inherent parent material strength (at the test temperature), the square of neck size ratio, sintered density, and particle packing coordination number.

2. Model development

Sintering involves heating a powder compact to a temperature where atomic motion leads to bond growth between contacting particles. Strength arises from the degree of bonding between contacting particles. Computer simulation allows calculation of the interparticle bond size and density in response to the sintering cycle (heating rate, temperature, hold time). Our model also considers the stress concentration associated with the neck of contacting particles, changing particle

coordination number with densification, and thermal softening of the material.

2.1. Computer simulation

Various transport mechanisms act simultaneously during sintering to deposit mass at the interface between adjacent particles [8]. Possible solid-state transport mechanisms include surface diffusion, volume diffusion from the surface, evaporation and condensation, grain boundary diffusion, plastic flow, dislocation climb, and volume diffusion from the particle contact area [1].

2.1.1. Calculation approach

The neck size ratio X/D and sintering shrinkage $\Delta L/L_0$ can be calculated through computer simulation. Here X is the diameter of the neck between contacting spheres of diameter D, L_0 is the initial length, and ΔL is the change in length. During sintering, the amount of material transported to the neck region is expressed by the following equation,

$$\frac{\mathrm{d}V_t}{\mathrm{d}t} = JA_r \tag{1}$$

where $\mathrm{d}V_t$ is the volume of material arriving at the neck during the time interval $\mathrm{d}t$, J denotes the flux of material moving into the neck, and A_r stands for the total area through which material passes. Thus, the neck growth rate is calculated by Equation 2:

$$\dot{X} = \frac{JA_r}{\left(\frac{\mathrm{d}V_t}{\mathrm{d}X}\right)} \tag{2}$$

To calculate the neck growth rate using Equation 2, geometric variables such as the contact area A_r, neck volume change $\mathrm{d}V_t$ with respect to neck growth $\mathrm{d}X$, and diffusion flux J must be known. Flux equations were derived previously [9, 10], and are summarized in Appendix A, while the geometric variables are calculated below.

2.1.2. Geometrical variables

Fig. 1 shows the two-sphere sintering model with specified geometric variables. Based on the method originally developed by German and Munir [11, 12] and an assumed circular neck shape, Sierra and Lee [13] calculated the neck volume V_t, as follows:

$$V_t = 2\pi\left[\left(\frac{X^2p}{4} + Xp^2 + \frac{5}{4}p^3\right)(1-\cos\phi) + \frac{2p^3 + Xp^2}{4}(\cos 2\phi - 1) + \frac{p^3}{12}(1-\cos 3\phi)\right] \tag{3}$$

The same method was used in other studies [9, 10, 14]. The angle ϕ can be calculated based on the relation

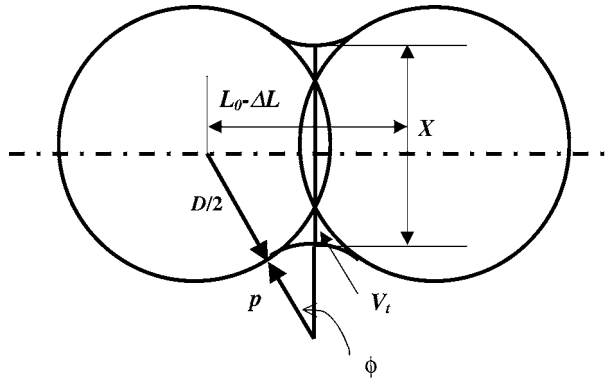

Figure 1 A schematic diagram showing the two-sphere sintering model with specified geometric variables.

defined in Fig. 1 as follows:

$$\sin\phi = \frac{L_0 - \Delta L}{2\left(p + \frac{D}{2}\right)} \tag{4}$$

where L_0 is the original center-to-center distance of the particles, and ΔL is the change in that distance due to densification. Geometry gives the following relation,

$$\left(p + \frac{D}{2}\right)^2 = \frac{1}{4}(L_0 - \Delta L)^2 + \left(p + \frac{X}{2}\right)^2 \tag{5}$$

To calculate the term $\mathrm{d}V_t/\mathrm{d}X$ in Equation 2, another equation is needed for volume conservation. The volume of the starting spheres is the same as the total volume of the particles and neck during sintering. Alternatively, the volume of mass arriving at the neck region is the same as the volume loss at the two contacting spheres. During densification, the contact area between the adjacent particles flattens due to shrinkage. Therefore, the volume loss V_1 at the spheres is given as follows,

$$V_1 = \frac{\pi}{3}\left(p\frac{L_0 - \Delta L}{(D_t/2) + p} + \frac{D_t}{2} - L_0 + \Delta L\right)^2 \times \left(D_t - p\frac{L_0 - \Delta L}{(D_t/2) + p} + L_0 - \Delta L\right) \tag{6}$$

where D_t is the particle diameter at any instant during sintering. Fundamentally there are two sources of mass to grow the sinter bonds—the particle surface (adhesion mechanisms such as surface diffusion) and the contact plane between the particles (bulk mechanisms such as grain boundary diffusion). For adhesion mechanisms, which give no shrinkage, the volume loss at the particles is caused by a reduction in particle diameter. Therefore, the volume loss V_2 can be expressed as follows:

$$V_2 = \frac{\pi}{6}\left(D^3 - D_t^3\right) \tag{7}$$

According to volume conservation during sintering,

$$\frac{1}{2}V_t = V_1 + \frac{1}{N_C}V_2 \tag{8}$$

where N_C is the particle coordination number. For adhesion mechanisms the coordination number N_C and interparticle distance L_0 are constant, while for densification mechanisms the particle diameter D remains unchanged, but particle coordination number N_C and interparticle distance L_0 change. Typically the volume conservation boundary condition and geometric relations are used along with mass transport models and material parameters to calculate the progressive microstructure and density changes during sintering.

2.1.3. Model implementation

When the values of A_r and dV_t/dX are computed for each transport mechanism, the neck growth rate equation defined by Equation 2 can be applied. According to the method used previously [9, 10, 13, 14], these rate equations are computed separately for densification and adhesion mechanisms. The instantaneous neck growth rate contributions from all adhesion mechanisms is computed using the relation suggested by Hwang and German [9],

$$\dot{X}_a = \dot{X}_{sd} + \dot{X}_{ec} + \dot{X}_{va} \tag{9}$$

where the subscript a represents adhesion mechanisms, and sd, ec, and va stand for surface diffusion, evaporation-condensation, and volume diffusion from the particle surface, respectively. As sintering time proceeds in an interval of Δt, the new value of neck size is calculated using Equation 10,

$$X_{new} = X_{old} + \dot{X}_a \Delta t \tag{10}$$

The new system geometry is then updated based on the calculated new neck size. The next step is to calculate the instantaneous neck growth rate contributions from densification mechanisms,

$$\dot{X}_d = \dot{X}_{gb} + \dot{X}_{vd} \tag{11}$$

where the subscript d represents densification mechanisms, and gb and vd represent grain boundary diffusion and volume diffusion from the interparticle grain boundary, respectively. Accordingly, the neck size is updated by the expression,

$$X_{new} = X_{old} + \dot{X}_d \Delta t \tag{12}$$

Knowing the geometry changes caused by both the adhesion and densification mechanisms, the simulation proceeds to the next time interval Δt and repeats the procedure. The geometric limit for the initial stage is the half-cone formula proposed by German and Munir [11, 12]. When the limit is reached, the angle ϕ as defined in Fig. 1 satisfies the following relation,

$$\phi = \sin^{-1}\left(1 - \frac{2}{N_C}\right) \tag{13}$$

where N_C is the particle coordination number as determined by the fractional packing density.

TABLE I Material constants and diffusion data for Cu-10Sn bronze

Atomic volume: $1.76 \times 10^{-29} m^3$
Theoretical density: 8.88 g/cm^3
Melting point: 1230 K
Surface energy: 1.7 J/m^2
Activation energy for surface diffusion: 225 kJ/mol
Frequency factor times effective surface thickness for surface diffusion: $6.4 \times 10^{-11} m^3/s$
Activation energy for volume diffusion: 207 kJ/mol
Frequency factor for volumne diffusion: $6.0 \times 10^{-10} m^2/s$
Activation energy for grain boundary diffusion: 114 kJ/mol
Frequency factor times grain boundary thickness for boundary diffusion: $7.7 \times 10^{-15} m^3/s$
Activation energy for evaporation-condensation: 324 kJ/mol
Pre-exponential vapor pressure: 8.6×10^4 MPa

2.1.4. Neck growth and shrinkage results

Computer simulations were conducted to examine effects of sintering parameters, such as peak temperature, isothermal hold time, and heating rate on interparticle neck growth and densification. The simulation was conducted using SintWin (version 2.3, P/M Lab, Pennsylvania State University) [9–14]. Table I lists the material constants estimated for the Cu-10Sn bronze powder. Sintering simulations are very sensitive to the activation energies, which are sensitive to composition and impurities. For this work, the activation energies for surface diffusion and grain boundary diffusion were selected to give agreement between the simulated and experimental results. Due to the scarcity of diffusion data for bronze, diffusion data of copper were first used to estimate the activation energies. The reported activation energy for copper surface diffusion range from 200 kJ/mol to 235 kJ/mol [15], while that for grain boundary diffusion is in the range from 102 to 120 kJ/mol [16]. The selected activation energies for bronze (225 and 114 kJ/mol) were in the range of reported values for copper.

As examples of the simulation results, Fig. 2 shows the predicted neck size ratio (X/D) versus time for

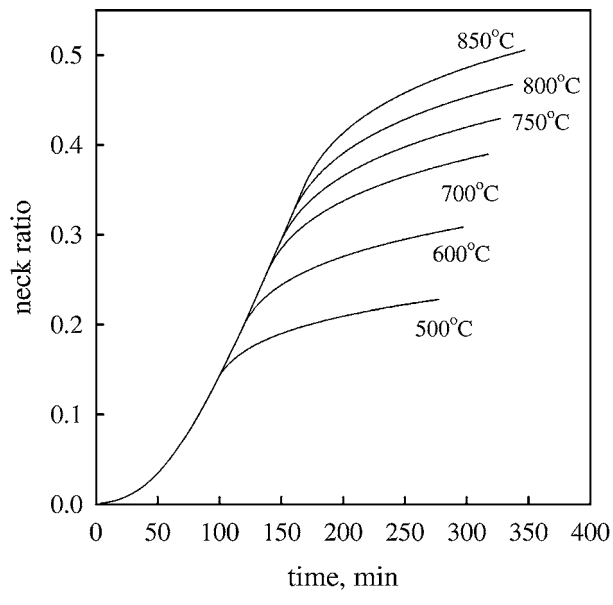

Figure 2 Simulation results of neck size ratio (X/D) versus times for 18 μm Cu-10Sn bronze powder with an initial fractional density of 55% heated from 20°C at 5°C/min and held at various peak temperatures.

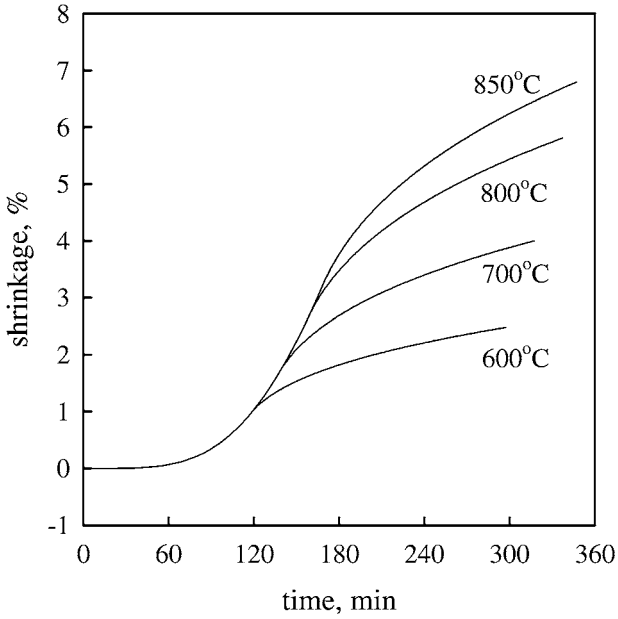

Figure 3 Simulation results of shrinkage ($\Delta L/L_0$) versus time for 18 μm Cu-10Sn bronze powder with an initial fractional density of 55% heated from 20°C at 5°C/min and held at various peak temperatures.

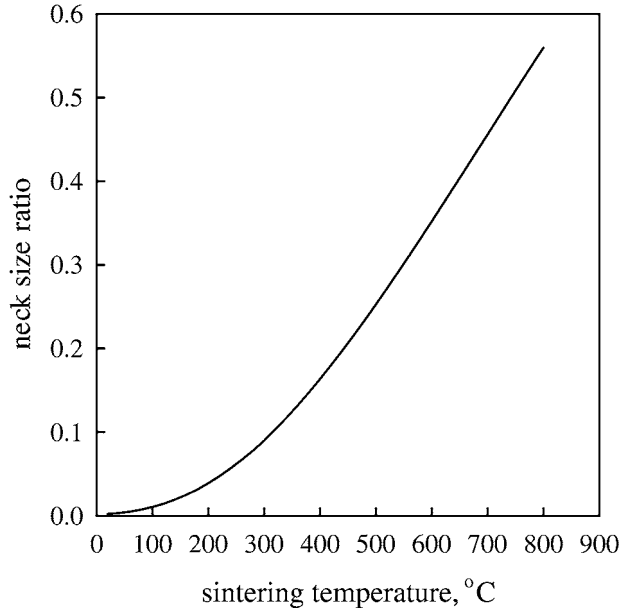

Figure 4 A plot of the simulated neck ratio (X/D) as a function of sintering temperature for mixed elemental Fe-2Ni-0.9C steel powder stating at 57% density with a 4 μm particle size, heated from 20°C at 5°C/min. Note no isothermal hold is employed in the simulation.

temperatures from 500 to 850°C. The time includes heating at 5°C/min and that of the isothermal hold. To match with the experimental study, the particle size was 18 μm and green density was 55% of theoretical. Fig. 3 plots the parallel shrinkage versus time results. These plots show an increase in sintering temperature and time improves interparticle neck growth and densification.

Similarly, computer simulation was performed on 4 μm mixed elemental Fe-2Ni-0.9C steel with a 57% green density to examine the effect of peak sintering temperature on interparticle neck growth and shrinkage. The simulation was run up to 800°C using a heating rate of 5°C/min, but was limited because the model does not allow for the phase transformation during heating. Table II shows the material constants and diffusion data applicable to α-Fe for the Fe-2Ni-0.9C steel. Again the activation energies for surface diffusion and grain boundary diffusion were adjusted to achieve agreement with the experimental data. The diffusion data were based on iron, due to lack of data for Fe-2Ni-0.9C (which is still largely an elemental blend during initial heating). The handbook activation energies for surface diffusion and grain boundary diffusion for α-Fe are 239 kJ/mol and 128 kJ/mol [1], respectively. Measured activation energy for surface diffusion for iron range from 176 to 250 kJ/mol [15], while that for grain boundary diffusion for α-Fe range from 105 to 180 kJ/mol [17, 18]. Moreover, the reported activation energy of grain boundary diffusion for Fe-5Ni was 115 kJ/mol [18]. Therefore, the selected values for surface diffusion and grain boundary diffusion (240 and 115 kJ/mol) were reasonable. Example simulation results of neck size ratio and shrinkage versus sintering temperature are shown in Figs 4 and 5, respectively. The results showed both neck growth and shrinkage increased with sintering temperature, with neck growth active at lower temperatures due to surface diffusion.

TABLE II Material constants and diffusion data for Fe-2Ni-0.9C steel

Atomic volume: 7.98×10^{-30} m^3
Theoretical density: 8.02 g/cm^3
Melting point: 1811 K
Surface energy: 1.95 J/m^2
Activation energy for surface diffusion: 240 kJ/mol
Frequency factor times effective surface thickness for surface diffusion: 2.7×10^{-9} m^3/s
Activation energy for volume diffusion: 251 kJ/mol
Frequency factor for volumne diffusion: 2.0×10^{-4} m^2/s
Activation energy for grain boundary diffusion: 115 kJ/mol
Frequency factor times grain boundary thickness for boundary diffusion: 1.73×10^{-14} m^3/s
Activation energy for evaporation-condensation: 340 kJ/mol
Pre-exponential vapor pressure: 7.4×10^4 MPa

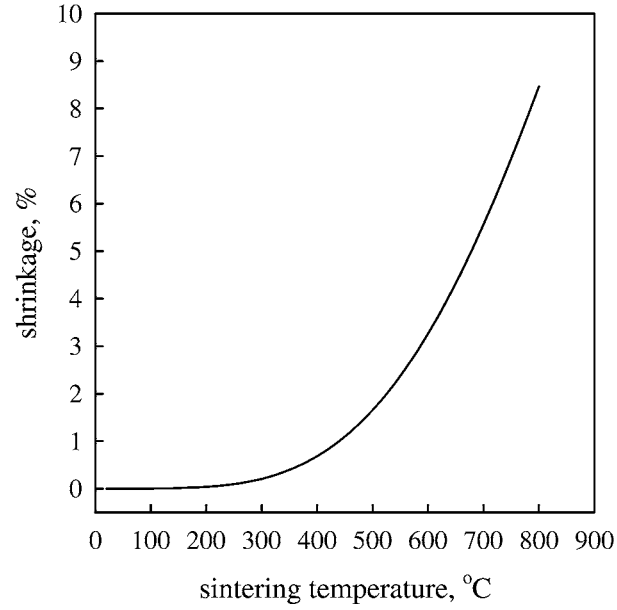

Figure 5 A plot of the simulated shrinkage ($\Delta L/L_0$) as a function of sintering temperature for 4 μm mixed elemental Fe-2Ni-0.9C steel powder starting with 57% green density and 20°C heated at 5°C/min. Note no isothermal hold is used in the simulation.

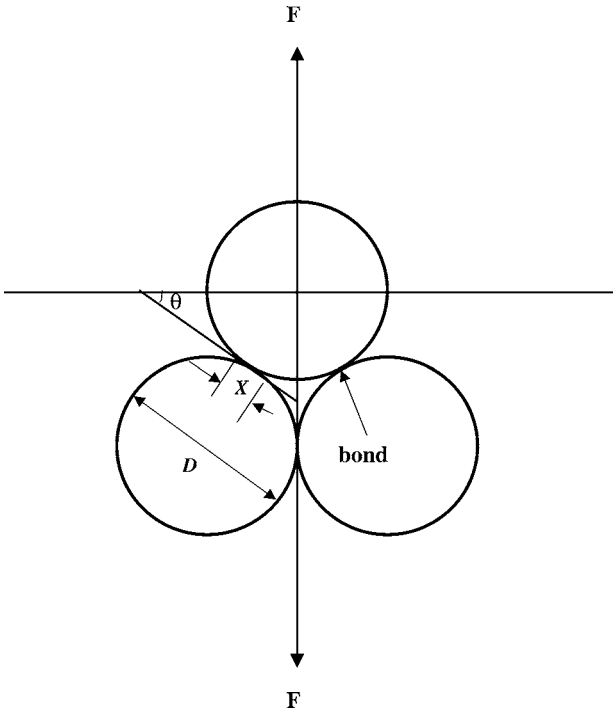

Figure 6 A schematic of clustered monosized spherical particles with diameter D and interparticle bond diameter X to show the resolved bond area in the plane normal to the tensile axis.

2.2. Strength model

Sintering reduces porosity and increases the interparticle bond size, thereby enhancing compact strength. In a powder compact, the bond between contacting particles or grains dictates strength. In developing the strength model, we assume monosized spherical particles. Fig. 6 shows a schematic of a three-particle cluster with particle diameter D and interparticle bond diameter X. Let θ be the angle between the bond plane and horizontal plane. An effective bond area is defined as a projected area into the horizontal plane, normal to an assumed vertical tensile loading. An effective bond area S_p is calculated as follows,

$$S_p = \left(\frac{\pi}{4}\right) X^2 \cos\theta \tag{14}$$

corresponding to a projection onto the plane normal to the tensile direction.

There are several interparticle bonds per particle. However, not all the bonds contribute to tensile strength. German [19] used a concept of effective number of bonds $N_{c,\text{eff}}$, which estimates the number of bonds fractured during a tensile test.

$$N_{C,\text{eff}} = \frac{N_C}{\pi} \tag{15}$$

where N_C is the average particle packing coordination number. Therefore, the total effective bond area $S_{p,\text{total}}$ can be calculated using Equation 16 as the product of the effective coordination number and individual effective bond area,

$$S_{p,\text{total}} = \left(\frac{N_C}{4}\right) X^2 \cos\theta \tag{16}$$

Hence, for each particle cluster, such as shown in Fig. 6, the ratio of total effective bond area and the projected particle is calculated as,

$$R = \frac{S_{p,\text{total}}}{S_{p,\text{particle}}} = \frac{\left(\frac{N_C}{4}\right) X^2 \cos\theta}{\left(\frac{\pi}{4}\right) D^2} = \left(\frac{N_C}{\pi}\right)\left(\frac{X}{D}\right)^2 \cos\theta \tag{17}$$

where $S_{p,\text{particle}}$ is the projected area of a particle on the horizontal plane. We assume the angle θ is randomly oriented among contacting particles. Considering there are many such particle clusters on the fracture surface, the ratio R can be computed using the following integration,

$$\int_0^{\frac{\pi}{2}} \left(\frac{N_C}{\pi}\right)\left(\frac{X}{D}\right)^2 \cos\theta \, d\theta = \left(\frac{N_C}{\pi}\right)\left(\frac{X}{D}\right)^2 \tag{18}$$

Due to a reduced load bearing area, the nominal strength of a porous material can be approximated as $\sigma_0 V_S$, where σ_0 is the strength of a wrought material and V_S is fractional density. Therefore, the strength of a sintered compact can be estimated as the product of the nominal strength and the ratio of total effective bond area to the projected particle area [19],

$$\sigma = \sigma_0 V_S \frac{N_C}{K\pi}\left(\frac{X}{D}\right)^2 \tag{19}$$

where σ is the measured strength and K is the stress concentration factor associated with the interparticle neck, which reduces the apparent bond strength. The stress concentration factor K is discussed in Appendix B. The solid coordination number is linked to the density for monosized spherical particle compacts as follows [1]:

$$N_C = 14 - 10.3(1 - V_S)^{0.38} \tag{20}$$

The *in situ* strength in sintering can be approximated by adding a thermal softening factor into Equation 19. An empirical thermal softening representation for 96% dense sintered bronze was given by a sigmoid function [6],

$$f_T = \frac{1.05}{1 + \exp\left(\frac{T - 720}{138}\right)} \tag{21}$$

where f_T is the remaining strength fraction, and T is the absolute temperature. Therefore, the *in situ* strength of a specimen is expressed as,

$$\sigma_0(T) = f_T \sigma_0 \tag{22}$$

where σ_0 is the strength of a wrought material at room temperature, and $\sigma_0(T)$ is the *in situ* strength of a wrought material at temperature T. Therefore, combining Equations 19, 20, and 22 gives a general form of *in situ* strength during sintering as follows:

$$\sigma_{\text{in situ}} = f_T \sigma_0 V_S \left(\frac{14 - 10.3(1 - V_S)^{0.38}}{K\pi} \right) \left(\frac{X}{D} \right)^2 \tag{23}$$

where $\sigma_{\text{in situ}}$ stands for the *in situ* strength of a compact at a test temperature T. Note this model predicts both the *in situ* strength and room temperature strength of a sintered structure, depending on the test temperature T. The neck size ratio X/D and solid fractional density V_S are determined by the sintering cycle and are based on computer simulations in this work.

3. Model testing

The strength model represented by Equation 23 was verified by comparing model predictions with experimental results reported in the companion paper [20]. The interparticle neck size ratio and sintering densification were obtained by computer simulation with input of various parameters as discussed earlier, including diffusion data, materials constants, and sintering parameters. The stress concentration factor K was estimated using the procedure shown in Appendix B. Comparisons between model predictions and measured strengths for Cu-10Sn bronze are shown in Figs 7 and 8, in which model predictions are in good agreement with the experimental results. The predicted and measured strengths were positively correlated (statistical significance greater than 99% confidence) at correlation coefficients of 0.98 and 0.99, respectively. The average difference between the experiment and model was 8.6% and 10.1%, respectively.

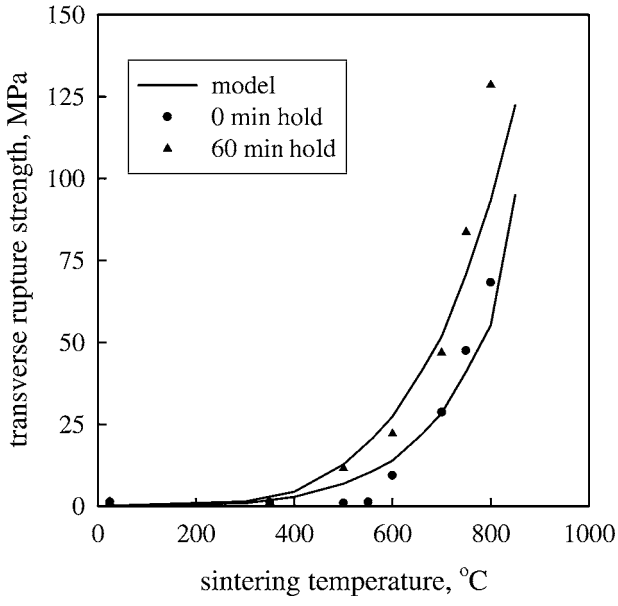

Figure 7 Experimental data and model predictions of room temperature transverse rupture strength versus peak sintering temperature (0 and 60 min hold) for 18 μm prealloyed Cu-10Sn bronze powder heated at 5°C/min in hydrogen.

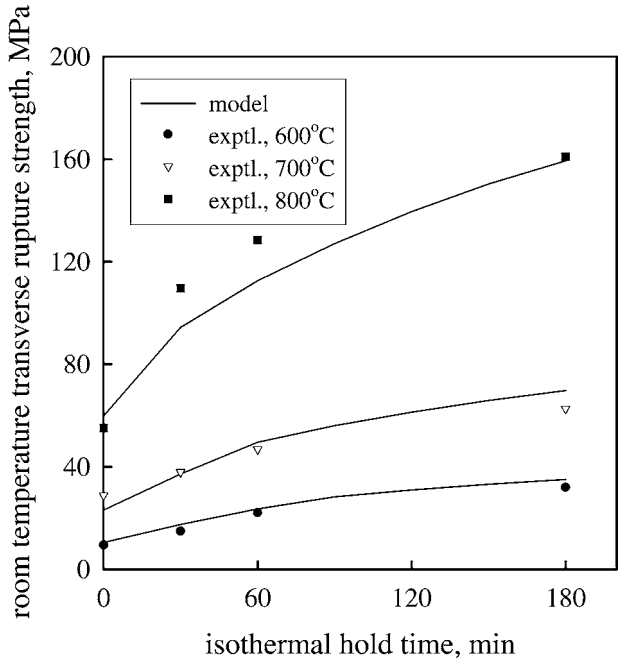

Figure 8 Model predictions compared with experimental results for the room temperature transverse rupture strength versus isothermal hold time for 18 μm prealloyed Cu-10Sn bronze powder heated at 5°C/min to the indicated temperature in hydrogen.

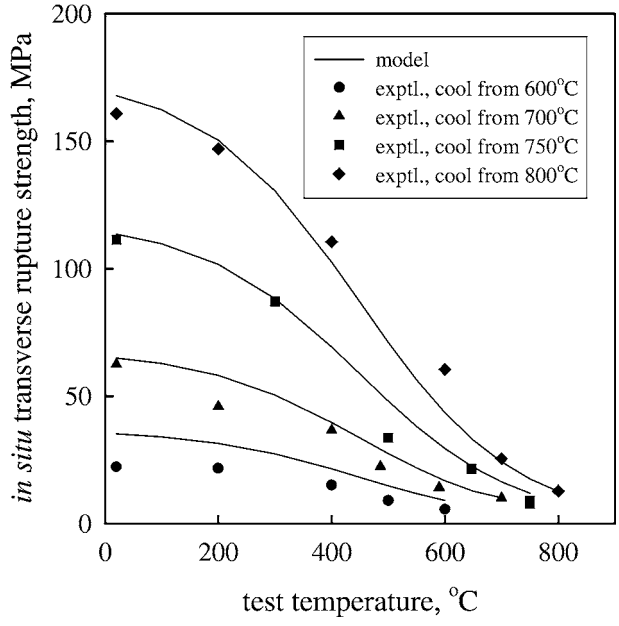

Figure 9 Model predictions of *in situ* transverse rupture strength during cooling from various peak sintering temperatures for 18 μm prealloyed Cu-10Sn bronze powder. Experimental data are plotted for comparison with model predictions.

The *in situ* strength data for the Cu-10Sn bronze obtained during cooling were used to further test the model predictions. The thermal softening behavior was obtained in a prior study [6]. Fig. 9 compares model predictions and experimental data during cooling, showing good agreement. A correlation coefficient of 0.99 was obtained, and the statistical significance was greater than 99%. The average deviation between model calculations and experimental data was 6.2%.

The model was further tested against experimental data for sintered mixed elemental powder Fe-2Ni-0.9C

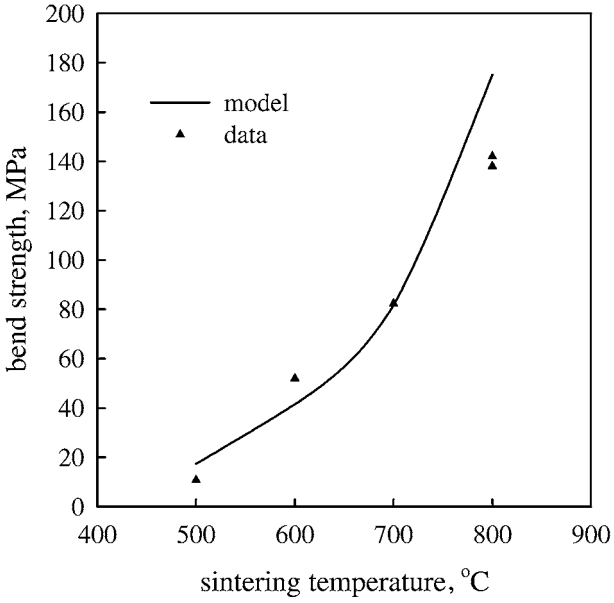

Figure 10 Model calculations of room temperature bend strength versus sintering temperature for 4 μm mixed elemental Fe-2Ni-0.9C steel powder heated at 5°C/min. Experimental data are included for comparison.

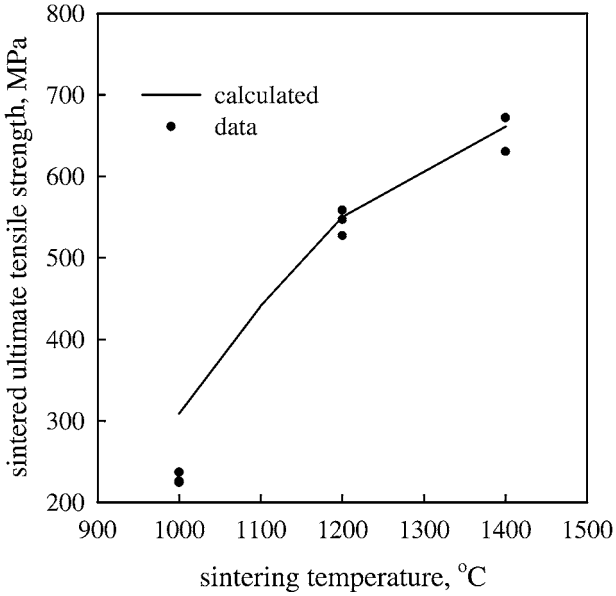

Figure 11 Model calculations of room temperature ultimate tensile strength versus sintering temperature for 4 μm mixed elemental Fe-2Ni-0.9C steel powder heated at 5°C/min. Experimental data are included for comparison.

steel. Fig. 10 compares sintered bend strength and model predictions based on computer simulated neck growth and densification. Computer simulation was performed up to 800°C. As shown in Fig. 10, good agreement was observed between the experimental data and calculations. The correlation coefficient was greater than 0.97, giving a statistical confidence greater than 99%. The average deviation between model calculations and experimental data was 18.2%. Figs 11 and 12 compare model calculated and measured room temperature ultimate tensile strength for the sintered Fe-2Ni-0.9C steel. Since the simulation was not extended into the γ-Fe region, the sintered neck size ratio was estimated from the sintered density V_S and initial fractional

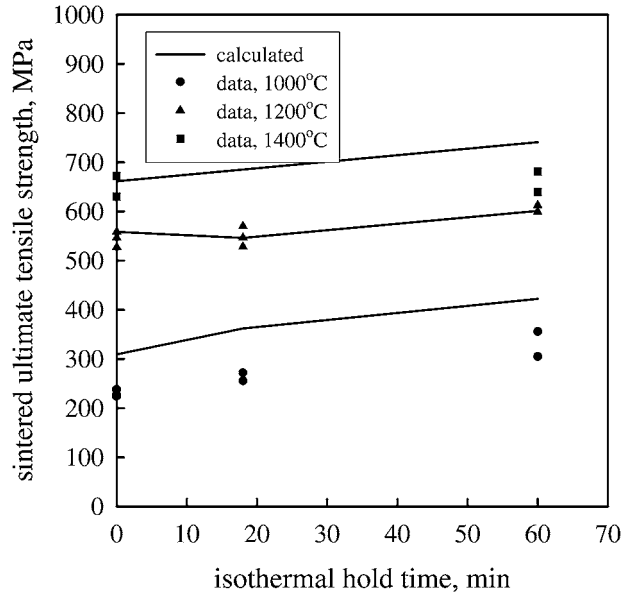

Figure 12 Model calculations of room temperature ultimate tensile strength versus peak temperature isothermal hold time for 4 μm mixed elemntal Fe-2Ni-0.9C steel powder heated at 5°C/min. Experimental data are included for comparison.

density V_O as the follows:

$$\left(\frac{X}{D}\right)^2 = 4\left[1 - \left(\frac{V_O}{V_S}\right)^{\frac{1}{3}}\right] \qquad (24)$$

Equation 24 is valid only for a neck size ratio smaller than 0.5. The model calculated ultimate tensile strength is in good agreement with experimentally measured data. The correlation coefficients were statistically signification with greater than 99% confidence at 0.99 and 0.98, respectively. Further, the average deviations between predicted and measured strengths in Figs 11 and 12 were 14.7% and 15.7%, respectively.

4. Discussion

The initial *in situ* strength of a compact in sintering emerges from the interparticle bonding between contacting particles. This is especially true during initial heating, since surface transport is favored at low temperatures, leading to bonding and strengthening with little densification [20]. The strength model given by Equation 23 demonstrates the importance of the interparticle neck size ratio (X/D). This effect of the neck size ratio on sintered strength is demonstrated in Fig. 13, a plot of sintered strength versus the square of neck size ratio for the Cu-10Sn bronze. Here the neck size ratios were obtained using computer simulation, while sintered transverse rupture strengths were measured experimentally. The plot in Fig. 13 shows an approximate linear relation between sintered strength and the square of neck size ratio, supporting the model. On the other hand, densification becomes evident at high sintering temperatures, further adding strength to the compact. Densification has a two-fold effect on strength. An increase in sintered density increases the net load-bearing section within the sintered structure as well as

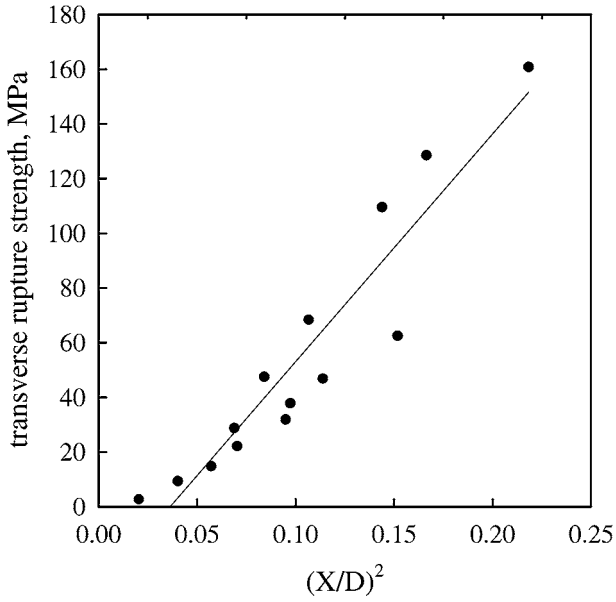

Figure 13 Experimental room temperature sintered transverse rupture strength versus the square of the neck size ratio $(X/D)^2$ for sintered 18 μm prealloyed Cu-10Sn bronze powder where the neck size is computer simulated for each sintering cycle. Even though this plot ignores density changes, the dominant role of neck size is apparent.

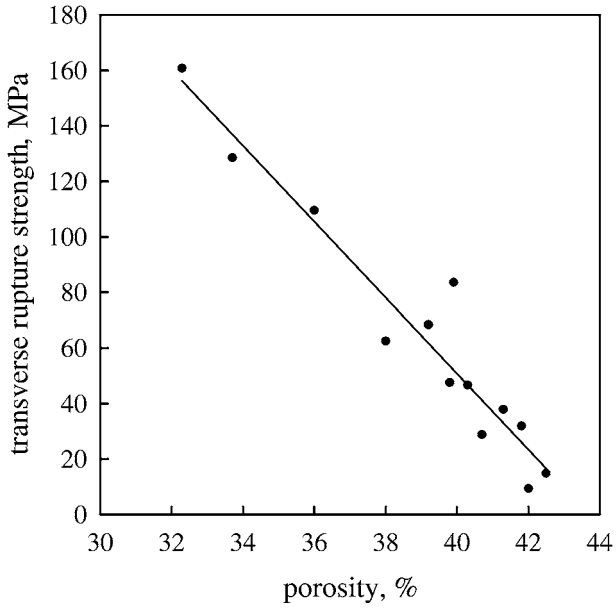

Figure 14 A plot of room temperature sintered transverse rupture strength versus porosity for various sintered 18 μm prealloyed Cu-10Sn bronze powder samples. In this case, the plot ignores neck size variations, yet illustrates the important role of compact density on strength.

the particle packing coordination number. Densification induces new particle-particle contacts, approaching a limit of 14 contacts per grain as full density is attained [1]. Fig. 14 shows a plot of sintered strength versus porosity for the bronze. As shown in the plot, sintered strength reduced with increasing porosity. The dependence of sintered strength on porosity is extensively documented for various materials in prior studies [21–26].

The strength model is verified by comparison between model predictions and experimental data for sintered bronze and steel powder compacts. Typical errors between the experimental data and model predictions are typically in the range of 10 to 15%. The model indicates two parameters dominate strength gains—the square of neck size ratio and fractional density. At low temperatures, compact strengthening for distortion and dimensional control needs to focus on promoting interparticle neck growth. However, thermal softening significantly decreases *in situ* strength at high temperatures, in the same temperature range where densification becomes active. Thus, thermal softening is a dominant factor that negatively impacts compact resistance to distortion and damage during sintering densification. Accordingly, excessive temperatures in sintering can cause excessive thermal softening, leading to distortion or loss of dimensional uniformity.

5. Conclusions

The strength of a sintered material is dominated by the interparticle neck size ratio (X/D) and fractional solid density (V_S). Significant neck growth occurs during initial heating at low temperatures, leading to an appreciable increase in strength often with little densification. Densification is favored by high sintering temperatures, and further contributes to sintered strength. On the other hand, thermal softening occurs at high temperatures, leading to a reduced *in situ* strength. This latter phenomenon is a major cause of distortion and loss of dimensional precision in sintering.

This strength model is developed for sintering powder compacts, which combines sintering theories and microstructure parameters, including interparticle neck size, solid volume fraction, and grain coordination. The model is verified by comparison with experimental data for a prealloyed Cu-10Sn bronze and mixed elemental Fe-2Ni-0.9C steel. The model can be extended to others systems. It demonstrates interparticle neck growth and densification are two key factors in determining sintered strength.

Acknowledgements

The National Aeronautics and Space Administration provided financial support for this research with supplemental support provided by the National Science Foundation. The authors would like to thank Dr. Yang Liu for help with computer programming.

Appendix A. Flux equations

For surface diffusion and grain boundary diffusion, the flux equations during sintering are based on the work of Kuczynski [27] and Johnson [28], respectively.

$$J = D_S \frac{\gamma \Omega}{kT} \frac{1}{p} \left(\frac{1}{p} - \frac{1}{X} + \frac{2}{D} \right) \tag{A1}$$

$$A_r = \pi X \delta \tag{A2}$$

$$J = 4 D_g \frac{\gamma \Omega}{kT} \left(\frac{X + p}{p X^2} \right) \tag{A3}$$

where D_S and D_g are the surface diffusion and grain boundary diffusion coefficients, γ is the surface energy, Ω is the atomic volume, k is Boltzmann's constant, and T is the absolute temperature, p is neck curvature radius, X is the neck diameter, D is the particle diameter, A_r is the area through which mass passes, and δ is the effective thickness of the surface layer or grain boundary thickness.

The flux equations for the evaporation and condensation, volume diffusion from the particle surface, and volume diffusion from the interparticle grain boundary were derived by Kingery and Berg [29], Kuczynski [27], and Johnson [28], respectively.

$$J = \alpha P \frac{\gamma\Omega}{kT}\frac{1}{\rho_t}\left(\frac{1}{p} - \frac{1}{X} + \frac{2}{D}\right)\left(\frac{M}{2\pi RT}\right)^{\frac{1}{2}} \quad \text{(A4)}$$

$$J = D_V \frac{\gamma\Omega}{kT}\frac{1}{p}\left(\frac{1}{p} - \frac{1}{X} + \frac{2}{D}\right) \quad \text{(A5)}$$

$$J = 4D_V \frac{\gamma\Omega}{kT}\left(\frac{X+p}{pX^2}\right) \quad \text{(A6)}$$

where P is the vapor pressure at a flat surface, M is the molecular weight of the material, ρ_t is the theoretical density of the material, D_V is the volume diffusion coefficient, and α is an accommodation coefficient and is taken as unity. The area can be expressed as follows [10]:

$$A_r = \pi p\left[\left(p + \frac{X}{2}\right)\arcsin\left(\frac{\sqrt{(D+2p)^2 - (X+2p)^2}}{D+2p}\right) - \rho\frac{\sqrt{(D+2p)^2 - (X+2p)^2}}{D+2p}\right] \quad \text{(A7)}$$

The above flux equations were used in prior studies [9, 10, 14]. In the present study, all transport mechanisms are considered to contribute to the neck growth simultaneously, while grain boundary diffusion and volume diffusion from the interparticle grain boundary are the mechanisms causing shrinkage.

Appendix B. Stress concentration factor

The elementary stress formulas used in the design of structural members are based on the members having a constant section or a section with gradual change of contour. However, such conditions are hardly ever attained in many structural members. The presence of shoulders, grooves, threads, and holes results in a localized high stress, known as stress concentration [30]. Similarly, there is a stress concentration at the neck region in sintered structures. The presence of stress concentration at the interparticle neck causes the measured strength of a sintered structure to be lower than the nominal material strength. The stress concentration factor K is defined as the ratio of the peak stress in the body (neck region) to the nominal stress,

$$K = \frac{\sigma_{max}}{\sigma_{nom}} \quad \text{(B1)}$$

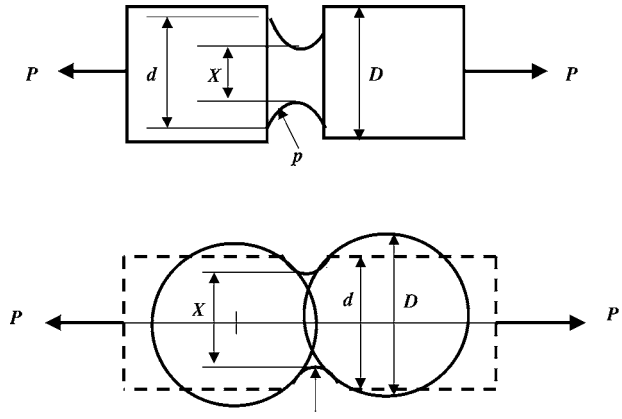

Figure 15 The schematic diagram showing the geometric profile of the neck, which is approximated as two circularly linked cyliders, and in the lower drawing this approximation is overlaid on the two particle sintering geometry.

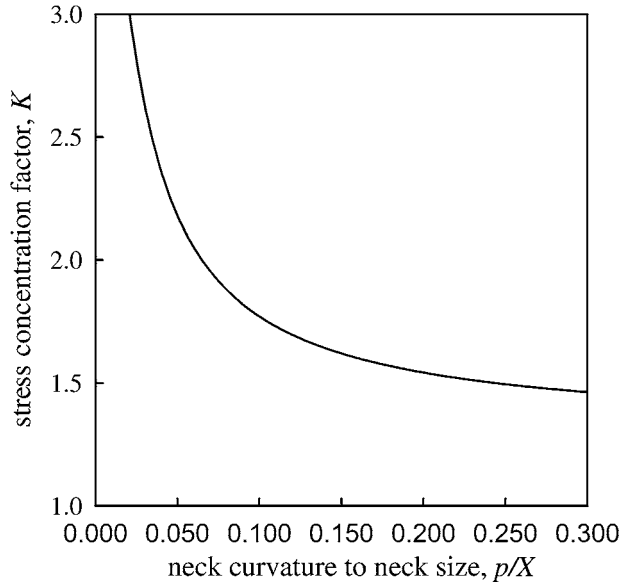

Figure 16 Stress concentration factor K for a tension bar of circular cross section with a U-shaped groove [30]. The circular neck between particles is approximated in this manner to estimate the stress concentration factor assuming $X/d = 1.05$.

where σ_{max} represents the maximum stress to be expected in the member under the actual load, and σ_{nom} is the nominal stress.

The circular profile of a neck region is schematically illustrated in Fig. 15. The neck between two sintered particles is comparable with two cylinders, which are circularly linked. The radius of the neck curvature is estimated as follows [31]:

$$p = \frac{X^2}{8D} \quad \text{(B2)}$$

where X is the diameter of interparticle neck, and D is the particle diameter. With the assumption of circular neck and $X/d = 1.05$, the stress concentration factor K is estimated using Fig. 16.

References

1. R. M. GERMAN, "Sintering Theory and Practice" (John Wiley & Sons, New York, NY, 1996).

2. *Idem*., "Particle Packing Characteristics" (Metal Powder Industrials Federation, Princeton, NJ, 1989).
3. I. H. MOON and J. S. CHOI, *Powder Metall.* **28** (1985) 21.
4. A. C. NYCE and W. M. SHAFFER, *Inter. J Powder Metall.* **8**(4) (1972) 171.
5. V. A. TRACEY, "Modern Developments in Powder Metallurgy," vol. 15, edited by E. N. Aqua and C. I. Whitman (Metal Powder Industries Federation, Princeton, NJ, 1985) vol. 15, 289.
6. G. A. SHOALES and R. M. GERMAN, "Metall. Mater. Trans. A," **29A** (1998) 1257.
7. *Idem*., *ibid.* **30A** (1999) 465.
8. M. F. ASHBY, *Acta Metall.* **22** (1974) 259.
9. K. S. HWANG, R. M. GERMAN and F. V. LENEL, *Powder Metall. Inter.* **23**(2) (1991) 86.
10. S. G. DUBOIS, M. S. Thesis, The Pennsylvania State University, University Park, PA, 1995.
11. R. M. GERMAN and Z. A. MUNIR, *Metall. Trans. B* **6B** (1975) 289.
12. *Idem., Metall Trans. A* **6A** (1975) 2229.
13. C. M. SIERRA and D. LEE, *Powder Metall. Inter.* **20** (1988) 28.
14. S. H. HILLMAN and R. M. GERMAN, *J. Mater. Sci.* **27** (1992) 2641.
15. G. NEUMANN and G. M. NEUMANN, "Surface Self-Diffusion of Metals" (Diffusion Information Center, Bay Village, OH, 1972).
16. I. KAUR, W. GUST and L. KOZMA, "Handbook of Grain and Interphase Boundary Diffusion Data" (Ziegler Press, Stuttgart, Germany, 1989) vol. 1.
17. E. A. BRANDES, (ed.), "Smithells Metals Reference Book," 7th edn. (Butterworth-Heinemann, Oxford, UK, 1992).
18. I. KAUR, W. GUST and L. KOZMA, "Handbook of Grain and Interphase Boundary Diffusion Data" (Ziegler Press, Stuttgart, Germany, 1989), vol. 2.
19. R. M. GERMAN, *Mater. Trans.* **42** (2001) 1409.
20. XIAOPING XU, WUWEN YI and R. M. GERMAN, *J. Mater. Sci*, to be published.
21. R. HAYNES, *Metal Powder Report* **46**(2) (1991) 49.
22. *Idem*., *Powder Metall.* **14** (1971) 64.
23. E. NAVARA and B. BENGTSSON, *Inter. J. Powder Metall. Powder Technol.* **20**(1) (1984) 33.
24. L. CIFUENTES and A. J. FLETCHER, *ibid.* **20** (1984) 51.
25. S. JAISWAL, A. J. FLETCHER and R. T. CUNDILL, *ibid.* **19** (1983) 51.
26. N. E. BAGSHAW, M. P. BARNES and J. A. EVANS, *Powder Metall.* **10**(19) (1967) 13.
27. G. C. KUCZYNSKI, *Trans. AIME* **185** (1949) 169.
28. D. L. JOHNSON, *Physics of Sintering* **1** (1967) 22.
29. W. D. KINGERY and M. BERG, *J. Appl. Phys.* **26** (1955) 1205.
30. W. D. PILKEY, "Peterson's Stress Concentration Factors," 2nd edn. (John Wiley & Sons, New York, NY, 1997).
31. J. L. JOHNSON, Ph.D. Thesis, The Pennsylvania State University, University Park, PA, 1994.

Received 28 November 2000
and accepted 28 August 2001